

Fabrication and research of bi-functional $CuNi_2S_4$ nanosheets decorated $TiO_2/CuNi_2S_4$ heterojunction photoanode for photoelectrochemical water splitting

Wei Jin(金伟), Liyuan Zhang(张立媛), Wenjing Zhang(张文静), Qian Sun(孙倩),Dekai Zhang(张德恺), Hui Miao(苗慧), and Xiaoyun Hu(胡晓云)
Citation: Chin. Phys. B, 2023, 32 (**11**): 118201. DOI: 10.1088/1674-1056/acef06
Journal homepage: http://cpb.iphy.ac.cn; http://iopscience.iop.org/cpb

What follows is a list of articles you may be interested in

Improving physical properties of poly(vinyl alcohol)/montmorillonite nanocomposite hydrogels via the Hofmeister effect

Rongrong Guo(郭蓉蓉), Deshuai Yu(余德帅), Yifan Huang(黄一帆), Sen Wang(王森), Cong Fu(付聪), Shuihong Zhu(朱水洪), Jia Yi(易佳), Hanqi Wang(王涵淇), and Youhui Lin(林友辉)
Chin. Phys. B, 2023, 32 (**8**): 088103. DOI: 10.1088/1674-1056/acdfc2

Enhanced xylene sensing performance of hierarchical flower-like Co_3O_4 via In doping

Jing Zhang(张京), Jianyu Ling(凌剑宇), Kuikun Gu(谷魁坤), Georgiy G. Levchenko, and Xiao Liang(梁霄)
Chin. Phys. B, 2023, 32 (**6**): 068104. DOI: 10.1088/1674-1056/acbe30

Tuning the particle size, physical properties, and photocatalytic activity of Ag_3PO_4 materials by changing the Ag^+/PO_4^{3-} ratio

Hung N M, Oanh L T M, Chung D P, Thang D V, Mai V T, Hang L T, and Minh N V
Chin. Phys. B, 2023, 32 (**3**): 038102. DOI: 10.1088/1674-1056/ac84ce

Performance optimization of self-powered visible photodetectors based on Cu_2O/electrolyte heterojunctions

Zhi-Ming Bai(白智明), Ying-Hua Zhang(张英华), Zhi-An Huang(黄志安), Yu-Kun Gao(高玉坤), and Jia Liu(刘佳)
Chin. Phys. B, 2020, 29 (**12**): 128202. DOI: 10.1088/1674-1056/abab7b

In-situ characterization of electrochromism based on ITO/PEDOT:PSS towards preparation of high performance device

Xue-Jin Wang(王学进), Zheng-Fei Guo(郭正飞), Jing-Yu Qu(曲婧毓),Kun Pan(潘坤), Zheng Qi(祁铮), Hong Li(李泓)
Chin. Phys. B, 2016, 25 (**2**): 028201. DOI: 10.1088/1674-1056/25/2/028201

SPECIAL TOPIC — Celebrating the 100th Anniversary of Physics Discipline of Northwest University

Fabrication and research of bi-functional $CuNi_2S_4$ nanosheets decorated $TiO_2/CuNi_2S_4$ heterojunction photoanode for photoelectrochemical water splitting

Wei Jin(金伟), Liyuan Zhang(张立媛), Wenjing Zhang(张文静), Qian Sun(孙倩), Dekai Zhang(张德恺), Hui Miao(苗慧)[†], and Xiaoyun Hu(胡晓云)[‡]

School of Physics, Northwest University, Xi'an 710127, *China*

(Received 16 May 2023; revised manuscript received 28 July 2023; accepted manuscript online 11 August 2023)

As a traditional n-type semiconductor, TiO_2 has good UV absorption ability and stable physical and chemical properties. However, its wide band gap and low oxygen evolution reaction (OER) activity limit its application in the field of photoelectrochemical (PEC) water splitting. In this work, a type-II $TiO_2/CuNi_2S_4$ heterojunction photoanode is successfully constructed, which expanded the light absorption range to visible and enhanced the OER activity. Firstly, TiO_2 nanotubes (NTs) thin films are prepared on Ti substrates by two-step anodization, and then the bi-functional electrocatalytic material $CuNi_2S_4$ is grown on TiO_2 NTs in the shape of nanosheets (NSs) *in situ* by solvothermal method. As a bi-functional electrocatalytic material, $CuNi_2S_4$ has good visible light absorption property as well as OER catalytic activity. Compared with TiO_2, the IPCE value of $TiO_2/CuNi_2S_4$ is 2.59% at 635 nm, and that of TiO_2 is a mere 0.002%. The separation efficiency and injection efficiency increase from 2.49% and 31.52% to 3.61% and 87.77%, respectively. At 1.23 V vs. RHE, the maximum photocurrent density is 0.26 mA/cm^2, which is 2.6 times than that of TiO_2 (0.11 mA/cm^2), and can be maintained at 0.25 mA/cm^2 for at least 2 h under light illumination. Moreover, a hydrogen production rate of 4.21 μmol·cm^{-2}·h^{-1} is achieved within 2 h. This work provides a new idea for the application of TiO_2 in the field of PEC water splitting and the construction of efficient and stable photoelectronic devices.

Keywords: TiO_2, $CuNi_2S_4$, high stability, photoelectrochemical properties

PACS: 82.47.Jk, 81.07.–b, 85.35.Kt **DOI:** 10.1088/1674-1056/acef06

1. Introduction

With the continuous development of industry, the over-exploitation and use of energy cause environmental problems such as energy shortage and environmental pollution. Therefore, the development of sustainable and renewable energy sources is imminent.[1–4] Compared with fossil energy,[5] a series of new energy sources, such as hydrogen,[6] wind,[7] geothermal,[8] nuclear,[9] and tidal,[10] have green and renewable advantages. Among them, hydrogen energy, as a clean energy with high heat value, has been widely concerned by many scientists at home and abroad.[11–13] As we all know, solar energy is recognized as the most ideal source of energy. Therefore, how to use solar energy for efficient photoelectrochemical (PEC) water splitting to produce hydrogen has been extensively and deeply studied.[14–16] Therefore, choosing the right semiconductor material is of paramount importance.[17–21] As a traditional hot material, titanium dioxide has attracted much attention from scientists because of its wide application in many fields.

TiO_2 is a traditional n-type semiconductor with a variety of crystal types and good chemical and thermal stability.[22,23] Since Fujishima and Honda first used TiO_2 as photoanode in 1972, it has been found that titanium dioxide had excellent electronic and optical properties under ultraviolet irradiation.[24–27]

With the extensive and in-depth research on titanium dioxide by scientists, titanium dioxide has been found to have a variety of morphologies, such as nanotubes (NTs),[28] nanorods (NRs),[29] nanosheets (NSs),[30] nanospheres (NSPs),[31] and nanowires (NWs).[32] Compared with other TiO_2 nanomaterials, one-dimensional, highly ordered TiO_2 nanotube arrays structure not only has a larger internal surface area, but also has a very strong adsorption capacity.[33–35] In addition, highly ordered TiO_2 NTs prepared on Ti substrate by two-step anodization can perform charge transfer more quickly due to its unique vertical orientation, thereby inhibiting the recombination of electron–hole pairs and improving the photoelectric conversion efficiency.[36,37] However, due to its large band gap (anatase $E_g = 3.2$ eV, rutile $E_g = 3.0$ eV), the light absorption of TiO_2 NTs in the ultraviolet region is limited and solar energy cannot be fully utilized. At the same time, TiO_2 has poor photoelectrochemical properties due to its high photo-generated carrier recombination rate and low OER activity.

[†]Corresponding author. E-mail: huim@nwu.edu.cn
[‡]Corresponding author. E-mail: hxy3275@nwu.edu.cn

© 2023 Chinese Physical Society and IOP Publishing Ltd

Therefore, many attempts have been made to overcome these shortcomings. Strategies such as doping metal or nonmetal,[38] surface modification,[39] defect introduction[40] and heterostructure construction[41] are employed. Among them, the construction of heterojunctions by composing other materials with TiO_2 has been proven to be an effective method to improve its photochemical properties. Materials used for this strategy include metal oxides (CuO,[42] Bi_2O_3,[43] In_2O_3[44]), metal sulphides and selenides (Ni_2S_3,[45] Bi_2S_3,[46] CdS,[47] Sb_2S_3,[48] Sb_2Se_3[49]), $Co(OH)_2$,[50] graphene,[51,52] as well as some ternary and quaternary sulphides and selenides, such as $CoNi_2S_4$,[53] $CdIn_2S_4$,[54] and Cu_2AgInS_4.[55] For instance, Park compounded In_2S_3 on TiO_2 NTs by the hydrothermal method, which could well achieve the absorption of visible light and effective charge separation, thus improving the property of PEC.[56] Li compounded $SnIn_4S_8$ on TiO_2 NTs by the solvothermal method, which was found to have high stability and low impedance, contributing to the cathodic protection of Q235.[57]

As can be seen, bimetallic sulphides have improved structure and electrical conductivity compared to monometallic sulphides. They have received a lot of attention in recent years due to their strong light absorption in the visible light absorption range and their good electron transport properties and stability. As a bimetallic sulfide, $CuNi_2S_4$ has a unique spinel structure which enables it to have high light ability. $CuNi_2S_4$ has a narrow band gap of 2.46 eV, which allows it to absorb ultraviolet and visible light.[58–61] In addition, as an electrocatalytic material, the synergistic effect of Ni and Cu elements in $CuNi_2S_4$ enables it to have good conductivity, reduce film resistance, and further enhance its OER activity. The physical and chemical properties of nanomaterials are mainly determined by their size, structure and morphology. The unique nanosheets structure of $CuNi_2S_4$ could enhance absorption of visible light and provide more surface reaction active sites, thereby improving the PEC property. However, very little research has been done on $CuNi_2S_4$ in relation to photoelectrocatalysis. As a bi-functional material, $CuNi_2S_4$ has both OER catalytic activity and good visible light absorption properties, and the two properties of $CuNi_2S_4$ can well compensate for the two disadvantages of TiO_2 mentioned above. Therefore, the fabrication of TiO_2 with the bi-functional material $CuNi_2S_4$ to improve its PEC property is a reliable measure.

In this study, a novel $CuNi_2S_4$ NSs/TiO_2 NTs heterojunction thin films were synthesized by two-step anodization and solvothermal methods. The photoelectrochemical properties and mechanisms were systematically studied. The above work provided a new idea for further improving the PEC water splitting ability of TiO_2 photoelectrodes.

2. Experimental details

2.1. Materials

All the reagents were of analytical grade and used without further purification. Ammonium fluoride (NH_4F, $\geq$ 96.0%) and thiourea (CH_4N_2S, $\geq$ 99.0%) were obtained from Tianjin Damao Chemical Reagent Factory. Ethylene glycol (EG, C_2H_6O, $\geq$ 99.0%) and glycerol ($C_3H_8O_3$, $\geq$ 99.0%) were purchased from Chengdu Colon Chemical Co., Ltd. Nickel chloride hydrate ($NiCl_2{\cdot}6H_2O$, $\geq$ 99.0%) was supplied by Shanghai Aladdin Biochemical Technology Co., Ltd. Copper sulfate pentahydrate ($CuSO_4{\cdot}5H_2O$, $\geq$ 99.0%) was purchased from Tianzheng Fine Chemical Reagent Field, Jindong, Tianjin. Pure Ti (99.99%, 40 mm $\times$ 20mm $\times$ 0.2mm). All chemicals and reagents used in the experiment were analytical grade purity, which can be used directly without further purification. The water used for preparing electrolyte and washing in the whole process was deionized water.

2.2. Fabrication of TiO_2 NTs

Place Ti foil substrate was etched in 100 ml mixed solution ($HF:HNO_3:H_2O$ = 1:4:5) for 2 h, and then washed with deionized (DI) water and ethanol to successfully remove the residue. Titanium dioxide nanotubes were prepared *in situ* on Ti substrate by two-step anodic oxidation method with self-made equipment. Ti foil was used as anode and high-purity graphite rod as cathode, with a distance of 3 cm between them. In the electrolyte, containing 0.587 g NH_4F, 2 ml H_2O, 98 ml EG and 0.587 g NH_4F, 30 ml H_2O and 70 ml $C_3H_8O_3$, respectively, two-step anodic oxidation was carried out at 60 V for 1.5 h and 40 V for 4 h. After ultrasonic treatment at each step, in order to convert amorphous titanium dioxide into relatively stable anatase phase, the obtained samples needed to be transferred to a muffle furnace at 450 °C for heating for 2 h at a heating rate of 5 °C·min^{-1}.

2.3. Preparation of the TiO_2/$CuNi_2S_4$ heterostructure

First, the prepared TiO_2 was repeatedly washed with deionized water and dried for standby. Due to the conductivity of both sides of the titanium sheet, the side with better TiO_2 film formation was selected as the use side and placed in the autoclave lined with 100 ml polytetrafluoroethylene to make its four corners contact with the bottom and wall of the container to ensure its stability in the container. Based on the prepared TiO_2 thin film photoelectrode, the TiO_2/$CuNi_2S_4$ heterojunction was prepared by one-step solvothermal method. Then, 0.1498 g $CuSO_4 \cdot 5H_2O$ and 0.2852 g $NiCl_2{\cdot}6H_2O$ were put into a beaker containing 20 ml of deionized water, and fully mechanically stirred at room temperature for 10 min with a magnetic stirrer. Next, added 20 ml of prepared ethanol solution to the beaker, and continued to stir for 10 min to fully

mix the solution. Finally, 0.548 g of thiourea was added to the beaker, and then fully stirred for 10 min. The color of the solution changed from light blue to turquoise green, and then the mixed solution was transferred to the polytetrafluoroethylene lined autoclave for sealed heating. After the reaction, all $TiO_2/CuNi_2S_4$ heterojunction samples were washed with deionized water several times and kept dry at 60 °C. On the basis of reaction for 20 h, $TiO_2/CuNi_2S_4$ heterojunction samples were prepared by changing the temperature (including 160 °C, 180 °C, 200 °C). Then the reaction temperature was fixed at 180 °C, and the $TiO_2/CuNi_2S_4$ heterojunction was prepared by changing the time (including 20 h, 24 h, 28 h).

2.4. Characterization measurements

Without special instructions, all $TiO_2/CuNi_2S_4$ heterojunctions used for characterization were prepared at 180 °C for 20 h. Using the x-ray power diffractometer (Shimadzu, XRD-6000, Cu-$K\alpha$ Radiation, $\lambda = 0.154056$ nm) to analyze the crystal phase and crystal size of the sample, and analyze the crystal phase at the scanning rate of $0.1°{\cdot}s^{-1}$ in the range of diffraction angle of 10°–70°. The morphology and elemental composition of the sample were observed by JSM-6390A scanning electron microscope (SEM) equipped with energy dispersive x-ray spectroscopy (EDS). The microstructure and lattice structure of the samples were observed by transmission electron microscopy (TEM, Tecnai G2F20 S-double field emission transmission). The optical properties of the samples were measured and analyzed in the range from 200 nm to 1200 nm by using a UV-vis-NIR spectrophotometer (PerkinElmer Lambda 950). By x-ray photoelectron spectroscopy (XPS, ULVAC-PHI, PHI5000 VersaProbeII) with Al $K\alpha$ as an x-ray source and C 1s (binding energy 284.8 eV) was used as a reference calibration to analyze the chemical composition and corresponding element valence of the sample.

2.5. Photoelectrochemical measurements

The electrochemical workstation (Versa STAT 4, Princeton, USA) was used to measure the photoelectrochemical property (PEC) of the sample. The xenon lamp (Zolix, 300 W, Sirius 300 P) provided 100 $mW{\cdot}cm^{-2}$ (AM 1.5G) light intensity for the test sample surface as a light source at room temperature. The three-electrode structure composed of platinum wire (counter electrode, CE), optical electrode (working electrode, WE) with an exposure area of 0.785 cm^2 and saturated Ag/AgCl (reference electrode, RE) was put into a neutral electrolyte solution (0.5 M Na_2SO_4, pH = 7.0) for testing. All other tests were carried out in 0.5 M Na_2SO_4 neutral solution, except that the sacrificial agent containing 0.35 M Na_2SO_3 and 0.25 M Na_2S (pH = 12.5) was used to measure the charge separation efficiency and charge injection efficiency of the sample.

The linear sweep voltammetry (LSV) curve was drawn from −0.1 V to 0.8 V vs. RHE. Ag/AgCl electrode at a scanning speed of 100 $mV{\cdot}s^{-1}$. At 1.23 V vs. RHE, the incident photon to current conversion efficiency (IPCE) curve was measured using different single-wavelength light emitting diodes (LED light source, Zolix MLED4–3) and optical power meters (NOVA IIOPHIR, Israel). Under the open circuit and AM 1.5G light irradiation, the electrochemical impedance spectroscopy (EIS) was measured at the starting frequency of 100 kHz and the ending frequency of 0.01 Hz. The Mott Schottky (MS) diagram with an AC amplitude of 10 mV and frequency of 1000 Hz was obtained in the dark. Put the sample in the neutral electrolyte solution (0.5 M Na_2SO_4, pH = 7.0), and monitor the hydrogen generation online by GC-7900 gas chromatograph.

Details about formula transformation and computation are provided in the support information. Figure 1 is the preparation diagram of $TiO_2/CuNi_2S_4$ heterojunction.

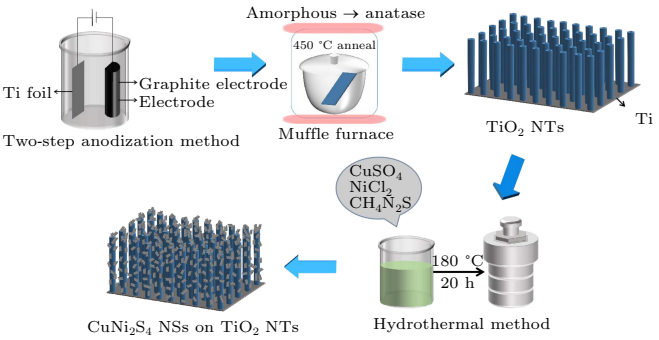


Fig. 1. Schematic diagram of preparation of $TiO_2/CuNi_2S_4$ composite photoelectrode.

3. Results and discussion

3.1. Morphology and structural characterization

The x-ray diffraction (XRD) of the monomer TiO_2 nanotube and $TiO_2/CuNi_2S_4$ composite sample is shown in Fig. 2. It can be seen that the TiO_2 monomer has a sharp and strong diffraction peak, indicating that the prepared monomer has good crystallinity. The six diffraction peaks at 25.37°, 37.05°, 37.91°, 48.16°, 54.05° and 55.20° correspond to the (101), (103), (004), (200), (105) and (211) crystal planes of anatase TiO_2 (JCPDS No. 73-1764), respectively, while the diffraction peaks at 35.33°, 38.68°, 41.15°, 52.90° and 63.26° respectively correspond well to the (100), (002), (101), (102) and (110) crystal planes of metal Ti (JCPDS No. 44-1294). It shows that TiO_2 photoelectrode material has been successfully prepared on Ti substrate by a simple two-step anodic oxidation method. In addition, after *in-situ* synthesis of $CuNi_2S_4$ by solvothermal method on the surface TiO_2 NTs, new diffraction

peaks are added. The diffraction peaks at 16.28° and 31.47° match the (111) and (311) crystal faces of the $CuNi_2S_4$ spinel phase (JCPDS No. 24-0334), and there are no other impurity peaks, indicating the $TiO_2/CuNi_2S_4$ heterojunction successfully constructed. The XRD plots of the monomeric $CuNi_2S_4$ (Fig. S1), prepared on ITO, show seven diffraction peaks at 16.3°, 26.7°, 31.5°, 38.1°, 47.2°, 50.2° and 55° that correspond to the (111), (220), (311), (400), (422), (511) and (440) crystallographic planes of $CuNi_2S_4$ (JCPDS No. 24-0334), respectively. This indicates that the preparation of $CuNi_2S_4$ monomer is successful.

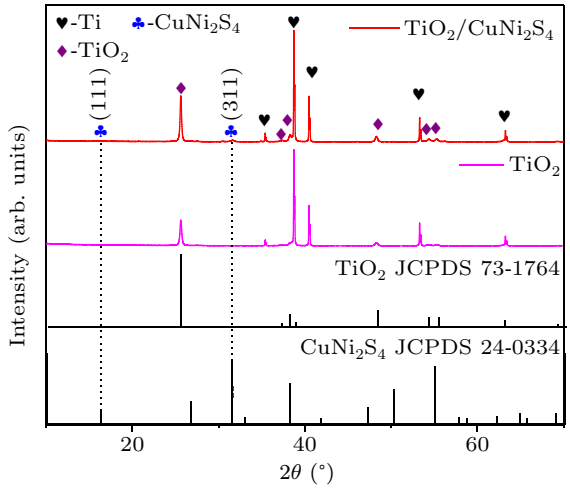


Fig. 2. XRD patterns for TiO_2 and $TiO_2/CuNi_2S_4$.

The prepared samples are characterized by scanning electron microscopy (SEM), and the morphology and distribution characteristics of pure TiO_2 nanotubes and $TiO_2/CuNi_2S_4$ heterojunction are observed. As shown in Fig. 3(a), the TiO_2 monomer film is composed of a number of smooth and flat nanotube arrays with a diameter of about 180 nm. Each nanotube is evenly distributed on the Ti substrate, indicating that the high-quality vertically grown TiO_2 NTs film was successfully prepared by two-step anodization. The unique structure of the nanotube can enable the electrons to carry out unidirectional transportation along the tube wall.[62] Therefore, the TiO_2 nanotube structure can simultaneously act as an electron transport layer to promote the transportation of photo-generated electrons, thus promoting the effective separation and transfer of photo-generated carriers. As can be seen from Fig. 3(b), retaining the original morphology of TiO_2 nanotubes, $CuNi_2S_4$ prepared by solvothermal method is connected on the surface of TiO_2 in the form of nanosheets, which increases the specific surface area and surface active sites, thus enhancing the light capture, absorption, and OER reaction kinetics. In addition, Fig. 3(b) also clearly shows that 2D $CuNi_2S_4$ NSs tend to self-assemble and grow randomly on 1D TiO_2 NTs along the inner and outer walls of nanotubes as well as pores. The EDS spectra of $TiO_2/CuNi_2S_4$ composite film in Fig. 3(e) prove the existence of Cu, Ni, S, Ti and O elements, and the uniform distribution of each element can be reflected from the corresponding element mapping image (Figs. 3(f)–3(j)).

The microstructure and morphology of $TiO_2/CuNi_2S_4$ are characterized by transmission electron microscopy (TEM). Figures 3(c) and 3(d) are TEM image of $TiO_2/CuNi_2S_4$ and their corresponding high-resolution transmission electron microscopy image (HRTEM), respectively. From Fig. 3(c), it can be seen that small $CuNi_2S_4$ nanosheets are wrapped around the TiO_2 NTs tube wall and also distribute on the TiO_2 NTs tube nozzle. In Fig. 3(d), a lattice stripe with a lattice spacing of 0.166 nm can be clearly observed at the TiO_2 NTs tube nozzle, which belongs to the (440) crystal plane of $CuNi_2S_4$. At the same time, a lattice stripe with a lattice spacing of 0.351 nm can be observed on the tube wall, which belongs to the (101) crystal plane of TiO_2.

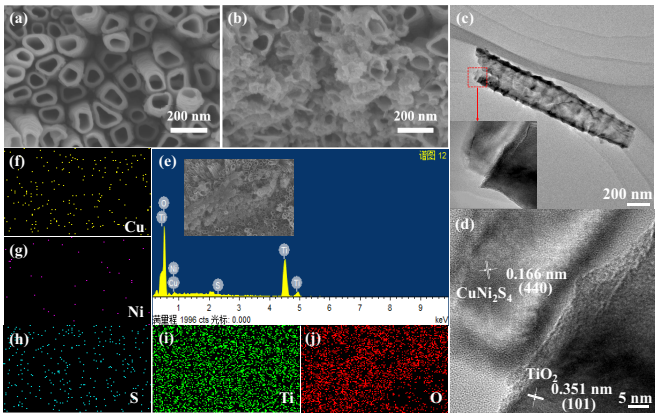


Fig. 3. (a) and (b) SEM images of TiO_2 and $TiO_2/CuNi_2S_4$. (c) and (d) The TEM and HRTEM images of $TiO_2/CuNi_2S_4$. (e) EDS spectra of $TiO_2/CuNi_2S_4$. (f)–(j) Elemental mapping images of $TiO_2/CuNi_2S_4$.

X-ray photoelectron spectroscopy (XPS) is used to further analyze the element composition and chemical valence. All measured peak positions are calibrated with reference to the binding energy (284.8 eV) of C 1s. As shown in the full spectra of all samples in Fig. 4(a), it is confirmed that there are Cu, Ni, S, Ti and O elements in the composite. In the high-resolution XPS spectra of Ti 2p (Fig. 4(b)), the two binding energy peaks at 458.67 eV and 464.34 eV can be attributed to the Ti $2p_{3/2}$ and Ti $2p_{1/2}$, indicating that the Ti ion is in the Ti^{4+} state in TiO_2.[63] Compared with the monomer TiO_2, the binding energy of Ti 2p in the $TiO_2/CuNi_2S_4$ heterojunction shifts negatively about 0.02 eV, and the spin–orbit splitting energy of Ti $2p_{3/2}$ and Ti $2p_{1/2}$ remains unchanged, which means that the Ti ion remains in the Ti^{4+} state. Figure 4(c) shows the peaks at 529.94 eV and 531.42 eV, corresponding to Ti–O–Ti bond (lattice oxygen) and H–O–H bond (adsorbed oxygen) of H_2O molecule adsorbed on the sample surface.[64] The position of the O 1s peak of the composite sample does not shift

after $CuNi_2S_4$ is decorated, which indicates that O 1s still exists in the form of hydroxyl.[65] The XPS pattern of Cu 2p in Fig. 4(d) shows four peaks at 931.83 eV, 933.46 eV, 951.53 eV and 954.89 eV. The peaks at 931.83 eV and 951.53 eV represent the Cu $2p_{3/2}$ and Cu $2p_{1/2}$ respectively, indicating that the Cu element has a +1 valence in $CuNi_2S_4$. The other two peaks at 933.46 eV and 954.89 eV correspond to the characteristic peaks of divalent copper, indicating that the element Cu also has a +2 valence in $CuNi_2S_4$. In the XPS pattern of Ni 2p (Fig. 4(e)), the peaks at 855.41 eV and 861.00 eV are Ni $2p_{3/2}$ characteristic peaks and corresponding satellite peaks, respectively. Meanwhile, the peaks at 873.43 eV and 879.77 eV are Ni $2p_{1/2}$ characteristic peaks and corresponding satellite peaks, respectively,[66] indicating that the valence state of Ni is +3. In Fig. 4(f), the two binding energy peaks at 161.06 eV and 162.27 eV can be attributed to S $2p_{3/2}$ and S $2p_{1/2}$, indicating that S ion is in the S^{2-} state. It can be seen from Figs. 4(d)–4(f) that the peaks corresponding to Cu, Ni and S elements in $TiO_2/CuNi_2S_4$ samples move slightly to higher binding energy in different degrees compared with pure $CuNi_2S_4$, and the increase of binding energy indicates that electrons flow from $CuNi_2S_4$ to TiO_2. In order to further study whether the composition and structure of $TiO_2/CuNi_2S_4$ heterojunction photoanode have changed, we further performed XRD and XPS tests on the composite photoelectrodes before and after the photoelectrochemical tests. The XRD patterns shown in Fig. S2(a) indicated that the diffraction peak positions and diffraction peak intensities of the composite photoelectrode before and after the PEC test had no significant change. The results showed that the composition of the composite photoelectrode had not changed. Meanwhile, a comparison of the elemental XPS high-resolution spectra of the composite photoelectrode before and after the test revealed that the fitted peak position and the fitted peak area were slightly changed (Figs. S2(b)–S2(f)). In addition, the presence of Ni^{2+} peak was found in the XPS high resolution spectra of Ni 2p. Through further investigation, it was found that this is because during the oxidation of water, Ni^{3+} in $CuNi_2S_4$ would first provide holes to the electrolyte and be reduced to Ni^{2+} itself. Subsequently Ni^{2+} would in turn receive holes from the $CuNi_2S_4$ valence band, which leads to its own oxidation to Ni^{3+}, thus forming a closed-loop reaction.

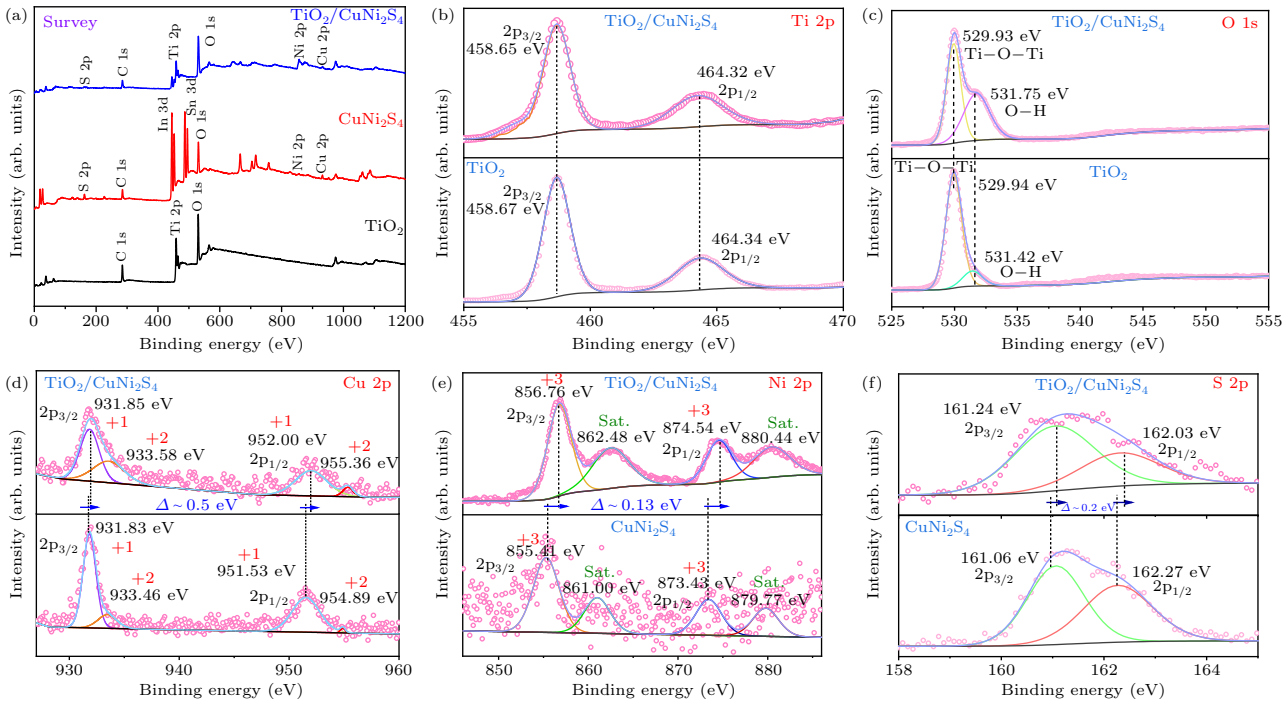


Fig. 4. (a) XPS survey spectra, (b) Ti 2p, (c) O 1s, (d) Cu 2p, (e) Ni 2p, and (f) S 2p high-resolution XPS patterns for pure TiO_2, $CuNi_2S_4$ and $TiO_2/CuNi_2S_4$ photoanodes grown on Ti substrate.

3.2. Optical absorption properties

The optical absorption characteristics of the sample are further characterized by UV-vis-NIR diffuse reflectance spectra. As shown in Fig. 5, the overall absorption strength of the composite sample is higher than that of the monomer TiO_2. Because the absorption band edge of $CuNi_2S_4$ (516 nm) is close to the absorption band edge of TiO_2 (382 nm), as shown in Fig. S3, the curve near the absorption band edge of TiO_2 NTs is generally steep, which makes the absorption band edge of $CuNi_2S_4$ is not very obvious. The absorption spectra of monomer $CuNi_2S_4$ are shown in Fig. S3(c). Compared with the TiO_2 NTs arrays uniformly arranged on the Ti substrate, $CuNi_2S_4$ grows randomly along the inner and outer walls of the nanotubes and nozzles on 1D TiO_2 NTs in the form of

nanosheets, which makes light reflect on the sample surface and further scatter to different angles, thus enhancing the ability of light capture and absorption of the sample. The band gap (E_g) is calculated by the following equation:

$$(\alpha h\nu)^n = A\left(h\nu - E_g\right), \tag{1}$$

where α is the absorption coefficient, $h\nu$ represents the energy of the incident photon, and A is a constant. When $n = 2$, it represents a direct band gap, and when $n = 1/2$, it represents an indirect band gap.[67] According to this formula, the band gaps of TiO_2 and $CuNi_2S_4$ are 3.2 eV and 2.46 eV as shown in Figs. S3(b) and S3(d), respectively.

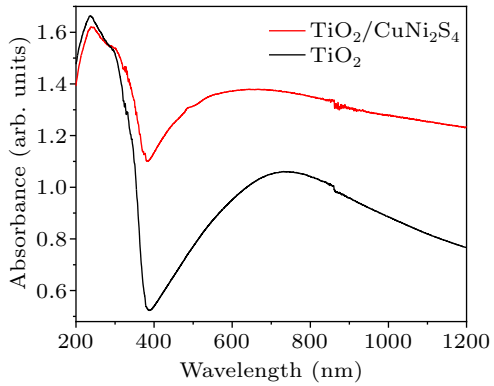


Fig. 5. UV-vis-NIR diffuse reflectance spectrum of TiO_2 and $TiO_2/CuNi_2S_4$.

3.3. Photoelectrochemical property of photoelectrodes

Under the irradiation of simulated sunlight (AM 1.5G), the photoelectrochemical properties of $TiO_2/CuNi_2S_4$ heterojunction photoanode are measured using a self-made PEC cell. The electrolyte in the test usually uses an aqueous solution containing 0.5 M Na_2SO_4. According to the theory of water oxidation potential,[68] when measuring the photoanode property of materials, the photocurrent density of electrodes at 1.23 V vs. RHE is usually used as the evaluation index of PEC property. Figure S4 shows the linear sweep voltametric curve (LSV) of $TiO_2/CuNi_2S_4$ prepared in the same solvent at different reaction temperature and time. It can be clearly seen from Fig. S4 that the shorter the reaction time, the lower the dark current of the composite sample. LSV and *J*–*t* curves have little overall change over time. The photochemical properties of a material are closely linked to its response to sunlight. The photocurrent density reflects the material's ability to respond to light, while the dark current density is related to the material's electrical conductivity. $CuNi_2S_4$, due to the introduction of Cu, has good electrical conductivity. However, to test the material's response to sunlight, it is advisable to select conditions that result in low dark current. Combined with all temperature and time gradients, the experiments show that $TiO_2/CuNi_2S_4$ prepared at 180 °C for 20 h has high photocurrent density and low dark current density, and its photocurrent current is about 0.26 mA/cm^2 (1.23 V vs. RHE). Compared with the monomer TiO_2 (0.11 mA/cm^2), it is 2.5 times higher (Fig. 6(a)). It is believed that $CuNi_2S_4$ is grown on the surface of TiO_2 nanotubes, which thus could effectively promote the transportation of photo-generated carriers. As is known, the stability is very important for the long-term PEC water splitting. Figure 6(b) shows the photocurrent density-time curve of $TiO_2/CuNi_2S_4$ composite photoelectrode tested for 2 h in 0.5 M Na_2SO_4 solution and under full open light. It can be seen that the $TiO_2/CuNi_2S_4$ composite sample prepared under the optimum reaction conditions of 180 °C for 20 h, whose photocurrent density first decreased and then stabilized at 0.25 mA/cm^2, which is about 2.5 times higher than that of TiO_2 monomer (0.11 mA/cm^2). The results show that the $TiO_2/CuNi_2S_4$ heterojunction photoanode has a high stability during the long-term PEC process. In order to make a more intuitive comparison of the PEC performance of $TiO_2/CuNi_2S_4$ photoanodes with that reported in other literature, Table S1 is presented. It can be seen from Table S1 that the performance of TiO_2 NTs photoanodes modified by bifunctional material $CuNi_2S_4$ is higher than that of TiO_2 photoanodes modified by other materials. It is well known that Ni ion has good catalytic activity. In the process of PEC water splitting, Ni^{3+} is reduced to Ni^{2+} as the reactive site, and Ni^{2+} is oxidized to Ni^{3+} by holes in the valence band of $CuNi_2S_4$, thus promoting the kinetics of OER reactivity. The combined effect of the elements Cu and Ni makes $CuNi_2S_4$ as a bi-functional material. It not only has good visible light absorption at the same time, but also has a good OER catalytic activity. Subsequently, the corresponding *J*–*t* curve and actual hydrogen production curve are obtained by continuously reacting for 2 h in a 0.5 M Na_2SO_4 neutral solution, as shown in Fig. S5. The $TiO_2/CuNi_2S_4$ heterojunction has been shown to have high stability and good hydrogen production capacity, as evidenced by the match between the theoretical and actual hydrogen production curves in Fig. S5. The sample has a hydrogen production rate of 4.21 μmol·cm^{-2}·h^{-1} and an average hydrogen production efficiency (η) of 91.48% within 2 h.

In order to further study the influence of the construction of $TiO_2/CuNi_2S_4$ heterojunction on the enhancement of photocurrent density, the bulk charge separation efficiency and surface charge injection efficiency of the sample are calculated (Figs. 6(c) and 6(d)). The solar spectrum and maximum theoretical photocurrent density of TiO_2 and $TiO_2/CuNi_2S_4$ curves are shown in Fig. S6. In Fig. 6(c), the bulk charge separation efficiency of $TiO_2/CuNi_2S_4$ is 3.61%, which is about 1.4 times than that of TiO_2 monomer (2.49%). The results

of bulk charge separation efficiency show that $TiO_2/CuNi_2S_4$ heterojunction can promote the separation of photo-generated electron–hole pairs, and finally improve the photocurrent response. It can be clearly seen from Fig. 6(d) that at 1.23 V vs. RHE, the injection efficiency of $TiO_2/CuNi_2S_4$ is as high as 87.77%, which is much higher than 31.52% of the monomer TiO_2. The above improvement of injection efficiency shows that the formation of $TiO_2/CuNi_2S_4$ heterojunction can effectively promote more photo-generated hole transport to the sample interface to participate in the oxidation reaction.

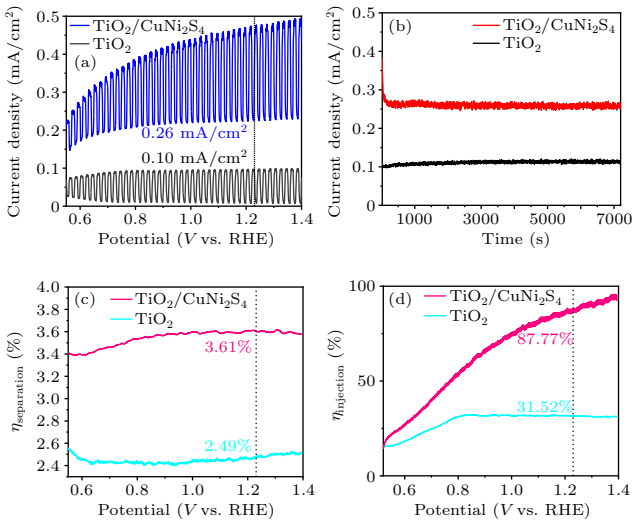


Fig. 6. (a) The *J*–*V* curves of $TiO_2/CuNi_2S_4$ heterojunction. (b) Two hours' stability diagram of $TiO_2/CuNi_2S_4$. (c) Charge separation efficiency and (d) charge injection efficiency of all samples.

In order to further study the interface charge transfer process, we use electrochemical impedance spectroscopy (EIS) to characterize the samples. EIS measurement is conducted under simulated AM 1.5G illumination and open-circuit voltage conditions. The measured arc radius is related to the charge transfer process at the corresponding electrode and electrolyte interface. Generally, the smaller the radius of the arc, the lower the transfer impedance of the electrode to the electrolyte. As shown in Fig. 7(a), the electrochemical impedance curves of the monomer TiO_2 and $TiO_2/CuNi_2S_4$ composite samples are semi-circular. In addition, the arc radius of $TiO_2/CuNi_2S_4$ composite sample is significantly smaller, which indicates that $TiO_2/CuNi_2S_4$ has a lower transfer resistance. This small transfer resistance is conducive to the migration of holes, thus promoting the water oxidation reaction ability at the interface. At the same time, the carrier lifetime of the sample can be calculated using the corresponding frequency of the characteristic peak in the Bode phase curve, as shown in Fig. S7, for the relevant calculation equation and test results. According to the relevant results tested (Fig. S7), the $TiO_2/CuNi_2S_4$ heterojunction (0.078 s) has a lower carrier lifetime compared to the monomeric TiO_2 (0.2 s). The lower carrier lifetime indicates that carriers can reach the surface of the object and the counter electrode faster to participate in redox reactions, reducing the chance of carrier recombination and thus improving PEC property.

In order to evaluate the ability of incident photons to convert into electrons, the ability of absorbing photons to convert into electrons (related to the light absorption of the material itself) and the ability of photons to convert into electrons under different bias voltages, the IPCE, APCE and ABPE curves of TiO_2 and $TiO_2/CuNi_2S_4$ heterojunction are calculated with reference to the supporting information (Eqs. S5–S7, IPCE, APCE and ABPE calculation formulas). As shown in Figs. 7(b) and 7(c), the IPCE and APCE values of $TiO_2/CuNi_2S_4$ at 635 nm are 2.59% and 2.82%, respectively. Meanwhile, the IPCE and APCE values of monomeric TiO_2 at 635 nm are 0.002% and 0.002%, respectively. Figure 7(d) shows the ABPE under different applied bias voltages. The maximum values (0.057% and 0.039%) are found at 0.85 V vs. RHE and 0.78 V vs. RHE for $TiO_2/CuNi_2S_4$ and TiO_2, respectively. These data indicate that the IPCE, APCE and ABPE values of $TiO_2/CuNi_2S_4$ are higher than those of monomeric TiO_2 under different single-wavelength light illumination and application of different bias conditions.

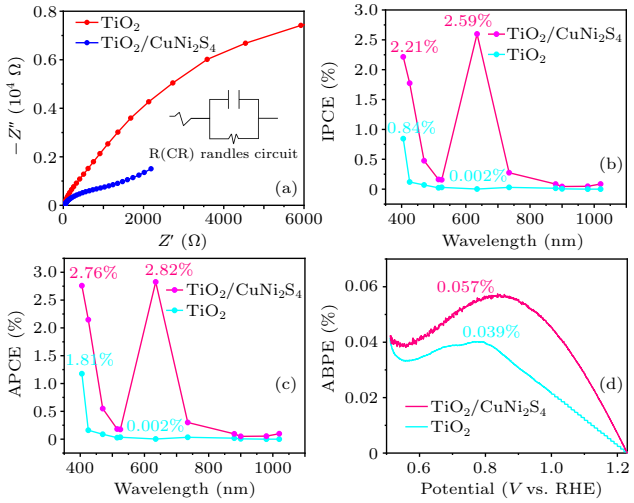


Fig. 7. Monomer TiO_2 and $TiO_2/CuNi_2S_4$ (a) Nyquist plots (EIS) under AM 1.5G illumination, the equivalent circuit model is shown in the illustration for data fitting, (b) IPCE spectra, (c) APCE spectra and (d) ABPE spectra.

Then, in order to verify the conductivity type and flat band potential (E_{fb}) of the prepared samples, the Mott–Schottky (MS) curves are measured under the dark condition with the test frequency of 1000 Hz. Figures 8(a) and 8(b) are the MS curves of TiO_2 monomer and $CuNi_2S_4$ monomer, respectively. It can be seen from the MS diagram that the tangents of the MS curves of TiO_2 and $CuNi_2S_4$ are both positive, indicating that they are n-type semiconductors. At the same time, the flat band potential (E_{fb}) of the sample can be calculated by using

the formula as follows:

$$\frac{1}{C^2} = \frac{2\left(E - E_{\rm fb} - \frac{KT}{e}\right)}{N_{\rm D} e \varepsilon \varepsilon_0}, \tag{2}$$

where C represents the space capacitance and e is the elementary charge quantity (1.6×10^{-19} C), ε_0 represents vacuum dielectric constant (8.85×10^{-12} F·m^{-1}), E is the applied bias voltage, $N_{\rm D}$ is the carrier concentration (cm^{-3}), $E_{\rm fb}$ is the flat-band potential, T is the temperature, and K is the Boltzmann constant (1.38×10^{-23} J·K^{-1}). Therefore, the flat-band potential ($E_{\rm fb}$) of TiO_2 and $CuNi_2S_4$ can be estimated to be 0.79 V and 0.69 V through the intersection of the tangent of the MS curve of the corresponding sample and the X axis. The relative distance between the Fermi energy level of the sample and the valence band of the semiconductor is measured by XPS valence band spectrum (Figs. 8(c) and 8(d)). Then, according to the position of Fermi energy level obtained by MS, the specific position of semiconductor valence band is deduced. As a result, the valence band ($E_{\rm v}$) of TiO_2 and $CuNi_2S_4$ can be deduced as 2.23 eV and 1.22 eV.

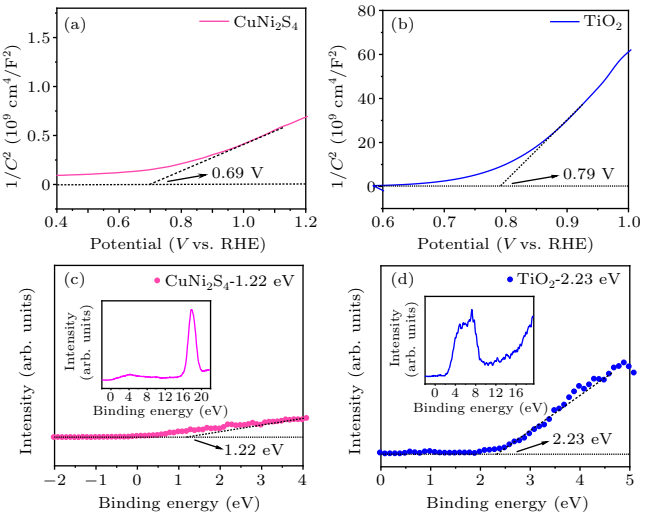


Fig. 8. Mott–Schottky curves of (a) $CuNi_2S_4$ and (b) TiO_2. XPS valance band spectra of (c) $CuNi_2S_4$ and (d) TiO_2.

In addition, the conduction band position of the monomer can be marked by the Tauc diagram of TiO_2 and $CuNi_2S_4$ in Figs. S3(b) and S3(d). According to the Fermi level and valence band position of semiconductor, a complete energy level structure diagram can be drawn to analyze the type of heterojunction formed. As shown in Fig. 9, the Fermi energy level of TiO_2 is more positive than that of $CuNi_2S_4$. When the two semiconductors contact, the Fermi level of TiO_2 moves upward and the Fermi level of $CuNi_2S_4$ moves downward until it reaches the equilibrium state. The energy band structure diagram of the TiO_2/$CuNi_2S_4$ heterojunction shows the characteristics of type-II scheme heterojunction. It can be seen that the electrons on the $CuNi_2S_4$ conduction band are more easily transferred to the TiO_2 conduction band, and then transferred to the counter electrode through the external circuit to participate in the reduction reaction. In addition, the holes on the TiO_2 valence band are transferred to the $CuNi_2S_4$ valence band, and then move to the surface of $CuNi_2S_4$ to participate in the oxidation reaction.

In order to better elucidate the charge transfer mechanism within the heterojunction, the mechanism diagram of PEC water splitting of TiO_2/$CuNi_2S_4$ was constructed (Fig. 10). Under the excitation of solar light, the electrons in the valence band of TiO_2 and $CuNi_2S_4$ were excited into the conduction band, thus leaving a large number of holes in the valence band. Meanwhile, electrons in the $CuNi_2S_4$ conduction band would be transferred to the counter electrode through the TiO_2 conduction band for hydrogen evolution reaction (HER) to produce hydrogen, while holes in the TiO_2 valence band would be transferred to the interface between the photoelectrode and the electrolyte through the $CuNi_2S_4$ valence band for OER to produce oxygen. Ni ion with good catalytic activity in $CuNi_2S_4$ promoted the kinetics of OER reaction. In addition, the construction of the typical type-II heterojunction could effectively realize the separation of photo-generated carriers, thus promoting the improvement of PEC water splitting property.

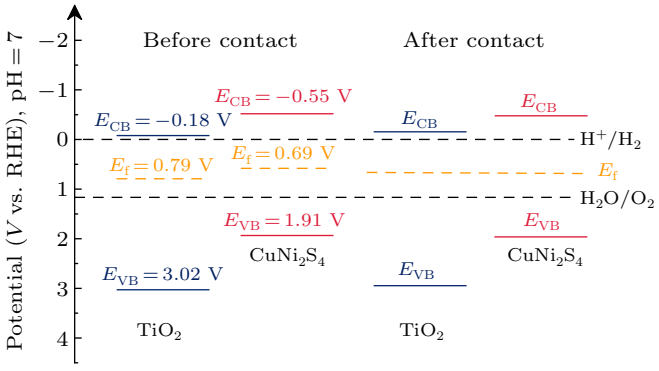


Fig. 9. The band gap structure of TiO_2 and $CuNi_2S_4$ before and after contact.

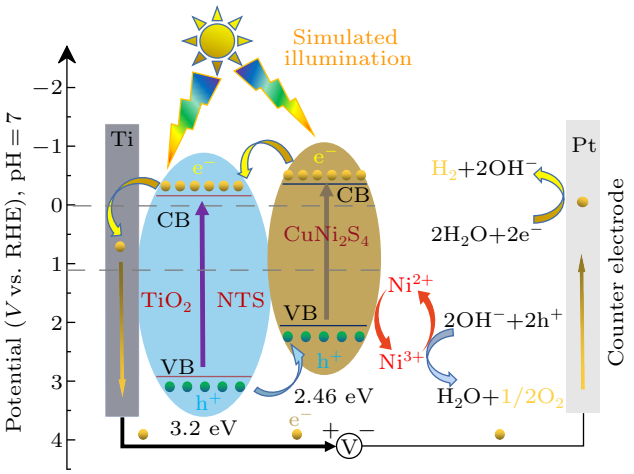


Fig. 10. The type-II scheme charge transfer mechanism between TiO_2 and $CuNi_2S_4$ under simulated light.

4. Conclusion

We had successfully prepared $TiO_2/CuNi_2S_4$ type-II heterojunction through a simple two-step anodic oxidation method and solvothermal method. The defects of TiO_2 itself were improved by exploiting the high OER activity and good visible light absorption properties of the bi-functional material $CuNi_2S_4$. The photocurrent density of the $TiO_2/CuNi_2S_4$ composite photoelectrode was 2.6 times higher than that of the TiO_2 monomer, and the composite photoelectrode still exhibited a photocurrent density of 0.25 mA/cm^2 (at 1.23 V vs. RHE) after 2 h of stability testing, demonstrating its high stability. At the same time, a stable hydrogen production rate (4.21 μmol·cm^{-2}·h^{-1}) was achieved in a continuous 2 h hydrogen production test. It was found that the enhancement of PEC property was mainly due to the efficient transportation channel of electrons by TiO_2 NTs, the formation of type-II heterojunction, and the good photostability of $CuNi_2S_4$ as an electrocatalytic material, as well as its high OER activity as a co-catalyst.

Acknowledgments

Project supported by the National Natural Science Foundation of China (Grant Nos. 11974276 and 11804274), the Natural Science Foundation of Shaanxi Province of China (Grant No. 2023-JC-YB-139), the Open Research Fund of State Key Laboratory of Transient Optics and Photonics, and the Chinese Academy of Sciences (Grant No. SKLST202211).

References

[1] Li S, Wang C, Cai M, Yang F, Liu Y, Chen J, Zhang P, Li X and Chen X 2022 *Chem. Eng. J.* **428** 131158
[2] Yang W and Moon J 2019 *ChemSusChem* **12** 1889
[3] Vickers N J 2017 *Curr. Biol.* **27** R713
[4] Mufutau O B 2021 *Energy* **228** 120519
[5] Leonard M D, Michaelides E E and Michaelides D N 2020 *Renew. Energ.* **145** 951
[6] Lebrouhi B E, Djoupo J J, Lamrani B, Benabdelaziz K and Kousksou T 2022 *Int. J. Hydrogen Energy* **47** 7016
[7] Liu L, Wang Y, Wang Z, Li S, Li J, He G, Li Y, Liu Y, Piao S, Gao Z, Chang R, Tang W, Jiang K, Wang S, Wang J, Zhao L and Chao Q 2022 *Resour. Conserv. Recycl.* **180** 106155
[8] Li Z, Luo Z, Wang Y, Fan G and Zhang J 2022 *Renew. Energ.* **184** 564
[9] Wang G, Chao Y, Jiang T and Chen Z 2022 *Sci. Total Environ.* **814** 151927
[10] Darmawi, Sipahutar R, Bernas S M and Imanuddin M S 2013 *Renew. Sust. Energ. Rev.* **17** 213
[11] Dawood F, Anda M and Shafiullah G M 2020 *Int. J. Hydrogen Energy* **45** 3847
[12] Sazali N 2020 *Int. J. Hydrogen Energy* **45** 18753
[13] Tarhan C and Çil M A 2021 *J. Energy Storage* **40** 102676
[14] Niu F, Wang D, Li F, Liu Y, Shen S and Meyer T J 2019 *Adv. Energy Mater.* **10** 1900399
[15] Arifin K, Yunus R M, Minggu L J and Kassim M B 2021 *Int. J. Hydrogen Energy* **46** 4998
[16] Reddy C V, Reddy K R, Shetti N P, Shim J, Aminabhavi T M and Dionysiou D D 2020 *Int. J. Hydrogen Energy* **45** 18331
[17] Guo X, Li M, Qiu L, Tian F, He L, Geng S, Liu Y, Song Y, Yang W and Yu Y 2023 *Chem. Eng. J.* **453** 139796
[18] Wang Y, Qiu L, Bao S, Tian F, Sheng J, Yang W and Yu Y 2023 *Sep. Purif. Technol.* **316** 123779
[19] Zhang X, Gao M, Qiu L, Sheng J, Yang W and Yu Y 2023 *J. Energy Chem.* **79** 64
[20] Zhang X, Gao M, Qiu L, Yang W and Yu Y 2023 *Chem. Eng. J.* **465** 142747
[21] Zhang X, Tian F, Lan X, Liu Y, Yang W, Zhang J and Yu Y 2022 *Chem. Eng. J.* **429** 132588
[22] Gao J, Xue J, Jia S, Shen Q, Zhang X, Jia H, Liu X, Li Q and Wu Y 2021 *ACS Appl. Mater. Interfaces* **13** 18758
[23] Zhang W, Xue J, Shen Q, Jia S, Gao J, Liu X and Jia H 2021 *J. Alloys Compd.* **870** 159400
[24] Lin S W, Tong M H, Chen Y X, Chen R, Zhao H P, Jiang X, Yang K and Lu C Z 2023 *ACS Appl. Energy Mater.* **6** 1093
[25] Hou J, Kong L, Xie Y, Ma J, Liu Y, Chen M and Wang Q 2022 *Ceram. Int.* **48** 3941
[26] Zhang S, Liu Z, Chen D, Guo Z and Ruan M 2020 *Chem. Eng. J.* **395** 125101
[27] Jia Y, Liu P, Wang Q, Wu Y, Cao D and Qiao Q A 2021 *J. Colloid Inter. Sci.* **585** 459
[28] Gao B, Sun M, Ding W, Ding Z and Liu W 2021 *Appl. Catal. B* **281** 119492
[29] Song X, Zhou H and Jiang C 2021 *Chin. Phys. B* **30** 058505
[30] Cheng Q, Yuan Y J, Tang R, Liu Q Y, Bao L, Wang P, Zhong J, Zhao Z, Yu Z T and Zou Z 2022 *ACS Catal.* **12** 2118
[31] Song Y, Waterhouse G I N, Han F, Li Y and Ai S 2021 *ChemCatChem* **13** 2931
[32] Zimbone M, Cantarella M, Impellizzeri G, Battiato S and Calcagno L 2021 *Molecules* **26** 1420
[33] Meng M, Li C, Li J, Wu J, Feng Y, Sun L, Yuan H and Liu K 2023 *J. Phys. D: Appl. Phys.* **56** 055502
[34] Tong M H, Wang T M, Lin S W, Chen R, Jiang X, Chen Y X and Lu C Z 2023 *Appl. Surf. Sci.* **623** 156980
[35] Xiao Z, Cheng S, Liao W, Fan D, Lu H and Liu Y 2022 *Int. J. Electrochem. Sci.* **17** 220817
[36] Frank A J, Kopidakis N and Lagemaat J V D 2004 *Coord. Chem. Rev.* **248** 1165
[37] Mor G K, Shankar K, Paulose M, Varghese O K and Grimes C A 2005 *Nano Lett.* **6** 215
[38] Hejazi S, Mohajernia S, Osuagwu B, Zoppellaro G, Andryskova P, Tomanec O, Kment S, Zboril R and Schmuki P 2020 *Adv. Mater.* **32** 1908505
[39] Park H, Park Y, Kim W and Choi W 2013 *J. Photoch. Photobi. C* **15** 1
[40] Jia G, Wang Y, Cui X, Zhang H, Zhao J, Li L H, Gu L, Zhang Q, Zheng L, Wu J, Wu Q, Singh D J, Li W, Zhang L and Zheng W 2022 *Matter* **5** 206
[41] Xu A, Tu W, Shen S, Lin Z, Gao N and Zhong W 2020 *Appl. Surf. Sci.* **528** 146949
[42] Singh J, Juneja S, Soni R K and Bhattacharya J 2021 *J. Colloid Interface Sci.* **590** 60
[43] Tang T, Yin Z, Chen J, Zhang S, Sheng W, Wei W, Xiao Y, Shi Q and Cao S 2021 *Chem. Eng. J.* **417** 128058
[44] Li Y, Wu Q, Chen Y, Zhang R, Li C, Zhang K, Li M, Lin Y, Wang D, Zou X and Xie T 2021 *Appl. Catal. B* **290** 120058
[45] Hou L, Bu Q, Li S, Wang D and Xie T 2016 *RSC Adv.* **6** 99081
[46] Ahmad A, Tezcan F, Yerlikaya G, Zia-ur-Rehman, Paksoy H and Kardaş G 2021 *J. Alloys Compd.* **868** 159133
[47] Kalanur S S, Lee S H, Hwang Y J and Joo O S 2013 *J. Photoch. Photobio. A* **259** 1
[48] Ito S, Tanaka S, Manabe K and Nishino H 2014 *J. Phys. Chem. C* **118** 16995
[49] Wang Y, Tang R, Huang L, Qian C, Lian W, Zhu C and Chen T 2022 *ACS Appl. Mater. Interfaces* **14** 33181
[50] Lu X, Liu L, Xie X, Cui Y, Oguzie E E and Wang F 2020 *J. Mater. Sci. Technol.* **37** 55
[51] Guo H, Jiang N, Wang H, Shang K, Lu N, Li J and Wu Y 2019 *Appl. Catal. B* **248** 552
[52] Zhao D, Sheng G, Chen C and Wang X 2012 *Appl. Catal. B* **111–112** 303

[53] Chen L, Zhou Y, Dai H, Yu T, Liu J and Zou Z 2015 *Nano Energy* **11** 697
[54] Zhu J, Cheng Y, Zhang W, Zhao J, Sun Q, Hu X and Miao H 2022 *Appl. Surf. Sci.* **601** 154188
[55] Kottayi R, Ilangovan V and Sittaramane R 2022 *Optik* **255** 168692
[56] Park J, Lee T H, Kim C, Lee S A, Choi M J, Kim H, Yang J W, Lim J and Jang H W 2021 *Appl. Catal. B* **295** 120276
[57] Li H, Song W, Cui X, Li Y, Hou B, Cheng L and Zhang P 2021 *Nano Energy* **16** 10
[58] Nouseen S, Singh P, Lavate S, Chattopadhyay J, Kuchkaev A M, Yakhvarov D G and Srivastava R 2022 *Catal. Today* **397–399** 618
[59] Mao M, Xu J, Yu X and Liu Y 2020 *Dalton Trans.* **49** 6457
[60] Adarakatti P S, Mahanthappa M, Hughes J P, Rowley-Neale S J, Smith G C, Ashoka S and Banks C E 2019 *Int. J. Hydrogen Energy* **44** 16069
[61] Zhu X and Liu S 2022 *J. Energy Storage* **51** 104582
[62] Yin Y, Li J, Wang Y, Wan J, Du X, Hu X, Liu E and Fan J 2017 *Mater. Res. Bull.* **88** 33
[63] Deng X, Zhang H, Guo R, Cui Y, Ma Q, Zhang X, Cheng X, Li B, Xie M and Cheng Q 2018 *Sep. Purif. Technol.* **193** 264
[64] Jiang X, Sun M, Chen Z, Jing J and Feng C 2020 *J. Alloys Compd.* **816** 152533
[65] Liu Q, Lu H, Shi Z, Wu F, Guo J, Deng K and Li L 2014 *ACS Appl. Mater. Interfaces* **6** 17200
[66] Hu J, Cao Y, Xie J and Jia D 2017 *Ceram. Int.* **43** 11109
[67] Chen C C, Shaya J, Polychronopoulou K, Golovko V B, Tesana S, Wang S Y and Lu C S 2021 *Nanomaterials* **11** 1325
[68] Dai X C, Huang M H, Li Y B, Li T, Zhang B B, He Y, Xiao G and Xiao F X 2019 *J. Mater. Chem. A* **7** 2741